Grain boundaries in chemical-vapor-deposited atomically thin hexagonal boron nitride

Xibiao Ren,[1] Jichen Dong,[2] Peng Yang,[3] Jidong Li,[4] Guangyuan Lu,[3] Tianru Wu,[3] Haomin Wang,[3] Wanlin Guo,[4] Ze Zhang,[1] Feng Ding,[2,5,*] and Chuanhong Jin[1,†]

[1]*State Key Laboratory of Silicon Materials, School of Materials Science and Engineering, Zhejiang University, Hangzhou, Zhejiang 310027, People's Republic of China*

[2]*Centre for Multidimensional Carbon Materials, Institute for Basic Science, Ulsan 44919, Republic of Korea*

[3]*State Key Laboratory of Functional Materials for Informatics, Shanghai Institute of Microsystem and Information Technology, Chinese Academy of Sciences, 865 Changning Road, Shanghai 200050, People's Republic of China*

[4]*State Key Laboratory of Mechanics and Control of Mechanical Structures, the Key Laboratory of Intelligent Nano Materials and Devices of DoE, Institute of Nano Science of Nanjing University of Aeronautics and Astronautics, Nanjing 210016, China*

[5]*School of Materials Science and Engineering, Ulsan National Institute of Science and Technology (UNIST), Ulsan 44919, Republic of Korea*

(Received 19 July 2018; revised manuscript received 10 October 2018; published 22 January 2019)

Atomically thin hexagonal boron nitride (h-BN) exhibits a wide band gap, as well as excellent thermal and chemical stability, and thus has been used in ultraviolet light emission and as building blocks for two-dimensional (2D) heterostructures. Large-area h-BN films for technical applications can now be produced by chemical vapor deposition (CVD). Unfortunately, grain boundaries (GBs) are ubiquitously introduced as a result of the coalescence of grains with different crystallographic orientations. It is well known that the properties of materials largely depend on GB structures. Here, we carried out a systematic study on the GB structures in CVD-grown polycrystalline h-BN monolayer films with a transmission electron microscope. Interestingly, most of these GBs are revealed to be formed via overlapping between neighboring grains, which are distinct from the covalently bonded GBs as commonly observed in other 2D materials. Further density functional theory calculations show that hydrogen plays an essential role in overlapping GB formation. This work provides an in-depth understanding of the microstructures and formation mechanisms of GBs in CVD-grown h-BN films, which should be informative in guiding the precisely controlled synthesis of large-area single-crystalline h-BN and other 2D materials.

DOI: 10.1103/PhysRevMaterials.3.014004

I. INTRODUCTION

Two-dimensional (2D) materials, such as graphene, hexagonal boron nitride (h-BN), and transition-metal dichalcogenides (TMDs), have attracted a great deal of interest because of their remarkable and technologically useful properties [1–3]. More interestingly, integrating these atomically thin crystals to heterostructures with a variety of properties opens up a new paradigm for nanoscale engineering [4,5]. Large-area, high-quality 2D materials are required for technical applications. Among numerous available synthesis methods, chemical vapor deposition (CVD) satisfies these demands and has been widely used to synthesis 2D materials because of its merits in controllability and low cost [6–8]. However, large-area CVD-grown 2D materials are typically polycrystalline and therefore inevitably contain grain boundaries (GBs), i.e., the interfaces between differently oriented grains. Most studies on GBs in 2D materials were based on the covalently bonded GB (CBGB) model in which two grains are covalently connected by topological defects along the GBs [9–13]. However, there is another type of GB: overlapping GBs (OLGBs) formed by one grain climbing upon another were also observed in 2D materials [14–19], but they attracted much less attention. The properties of the polycrystalline 2D films are largely influenced by the constituent grains and the structure of GBs [20–22]. Hence, distribution of CBGBs and OLGBs in the film should also be considered because of the different impacts of OLGBs on the properties of materials as compared with CBGBs, i.e., mechanical strength or thermal conductivity. Though much work has been done so far to reveal the GB structures in 2D materials, there are very few studies revealing the distribution of different types of GBs in CVD-grown films as well as bridging the atomic scale and grain scales of GBs to get the full picture of GB structure.

Atomically thin h-BN is a binary 2D compound with a lattice similar to that of graphene. It exhibits extraordinary properties, such as high mechanical strength [23] and good thermal conductivity [24], as well as excellent chemical stability [25,26]. It has been used in ultraviolet light emission [27] and serves as a fundamental building block for van der Waals heterostructures because of its atomically smooth surface [28,29]. Thus, it is essential to explore the GB categories and distinguish the primary GB structures in CVD-grown polycrystalline h-BN. Furthermore, understanding the formation mechanism of GBs in h-BN could also help to understand the GBs in other 2D materials

Here, we build a full picture of GB structures in CVD-grown monolayer h-BN by conducting dark-field imaging analysis at the grain size scale, and spherical

*f.ding@unist.ac.kr
†chhjin@zju.edu.cn

aberration-corrected high-resolution transmission electron microscopy (HRTEM) imaging to get the atomic structures. Our results show that OLGBs are found to be dominant in CVD-grown h-BN based on statistical analysis of over 100 GBs. We also explored the structure of GBs formed between two rotationally aligned grains, which shows a folded structure feature instead of the perfect connection between two grains. To obtain a deep understanding of the formation mechanism of OLGBs in h-BN, we carried out density functional theory (DFT) calculations and revealed the energetic competition between CBGBs and OLGBs responsible for the formation of GBs, and the role of hydrogen during the formation of GBs.

II. METHODS

A. Synthesis of h-BN samples

$Cu_{85}Ni_{15}$ alloy substrate was used for the CVD synthesis of h-BN domains as reported previously [30]. The introduction of Ni dramatically decreases the nucleation density of h-BN on the substrate and therefore increases the growing time of single crystals before they merge together, which results in large-size single-crystalline grains. Ammonia borane (H_3BNH_3) was used as the precursor for the growth of h-BN samples. The growth was carried out in a two-zone furnace. After the zone with $Cu_{85}Ni_{15}$ substrates reaches a temperature of 1070 °C, the zone containing the ammonia borane was gradually heated to 75 °C in 10 min. During the growth, the chamber pressure was kept at 20–100 Pa under 100 sccm H_2. Normally, the growth of discrete h-BN domains takes about 60 min while the growth of continuous h-BN film takes more than 90 min. After the growth, the furnace was quickly cooled down to room temperature under the protection of Ar flow.

B. TEM sample preparation and characterization

As-grown monolayer h-BN on a $Cu_{85}Ni_{15}$ substrate was spin-coated with poly(methyl methacrylate) (PMMA) and treated by oxygen plasma to remove the backside samples. The sample was then transferred onto a TEM grid (quantifoil with a pore size of 1.2 μm) and ultrathin carbon film using the electrochemical bubbling method [31]. Selected area electron diffraction (SAED) and HRTEM were done in a TEM (Titan G2 80-300, FEI) with a spherical aberration corrector on the imaging side and a monochromator that reduces the energy spread down to 0.12 eV. We used a positive spherical aberration (C_3) of 5 μm and a negative defocus of around −5.6 nm for atomic-resolution HRTEM. To reduce the radiation damage, this microscope was operated at an acceleration voltage of 80 kV and a dose rate of about 1×10^6 e/nm^2 s. All the HRTEM images were processed to remove the illumination variation with a band-pass filter by Image J. Electron energy loss spectroscopy (EELS) experiments were conducted with a Gatan Quantum 963 spectrometer in diffraction mode. Secondary-electron scanning electron microscope (SEM) images were collected in a Hitachi SU70 at 3 kV.

C. Density functional theory calculations

First-principles density functional theory (DFT) calculations were carried out using the Vienna ab initio simulation Package (VASP) [32,33]. The interaction between the valence electrons and ion cores was treated by the projected augmented wave (PAW) method [34]. The Perdew-Burke-Ernzerhof generalized gradient approximation (GGA) was chosen for the exchange-correlation interaction [35]. In addition, to describe the weak van der Waals interaction between h-BN layers and the substrate, the DFT-D2 method was used [36]. The energy cutoff for the plane-wave basis was set as 400 eV.

To model the structures of various h-BN edges and grain boundaries (GBs) on Cu substrate, a Cu(111) slab consisting of three atomic layers was constructed as the substrate, of which the unit-cell size was $6.65 \times 34.56 \times 20.81$ Å^3 and the bottom layer was fixed to mimic the bulk Cu foil. Due to the lattice mismatch between h-BN and Cu, the lattice constant of the Cu substrate has already been reduced by less than 4% to remain commensurate with h-BN. To model the formation of h-BN GBs, a pair of twin h-BN ribbons placed on a Cu substrate was used. Their edges are either passivated by H or by the substrate. The k-point mesh was sampled as $5 \times 1 \times 1$. All the structures were optimized until the force on each atom is within 0.01 eV/Å.

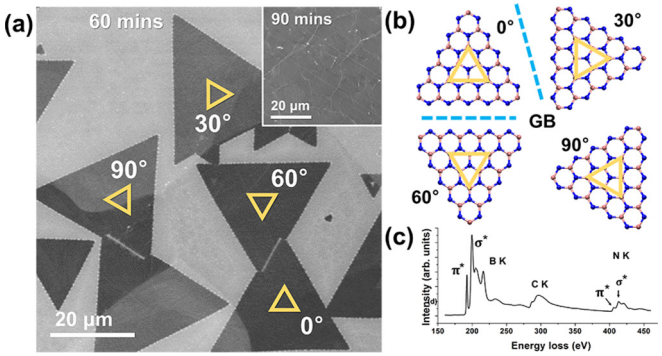

FIG. 1. (a) Secondary-electron SEM images of h-BN samples containing both discrete triangular grains and continuous film (inserted). The yellow triangles represent their crystallographic orientations. Note that 0° is an arbitrary value relative to other orientations. (b) Schematic illustration of the orientations of the h-BN domains. The blue dashed lines indicate the location of grain boundaries resulting from grains with two different orientations. Red balls represent B atoms and blue balls denote N atoms. (c) The core-loss EEL spectra, where both B and N are identified. Note that the C K-shell signals are coming from the ultrathin carbon film served as the TEM supports. More sample information is displayed in Fig. S1 and S2 in the Supplemental Material [37].

III. RESULTS

A. Structures and statistics of grain boundaries

We adopt two types of h-BN samples grown on Cu-Ni alloy ($Cu_{85}Ni_{15}$) substrates with a (100) dominated crystallographic facet at two different growth times (60 min for discrete film and 90 min for continuous film, respectively), as shown in Fig. 1(a). The triangular shaped h-BN grains displayed in Fig. 1(a) indicate that these grains are single crystals with nitrogen-terminated zigzag edges [38]. Due to the fourfold symmetry of the metal substrate and the epitaxial growth of

h-BN on the substrate, there are four primary orientations of the h-BN grains [39] as marked with yellow triangles in Fig. 1(a), leading to the formation of GBs with two orientations, as shown in Fig. 1(b). In addition to the GBs with a misorientation angle of 30°, there is an inversion GB between two joint grains with a misorientation angle of 60°, due to the polar structure of h-BN with alternating boron and nitrogen atoms in a honeycomb arrangement. Furthermore, it is feasible to find the interface between two unidirectionally aligned h-BN grains in the samples, which is usually considered to be perfect, if the relative sliding of the two grains is ignored. Therefore, the samples used can serve as an ideal platform for a systematic study of the GBs in CVD-grown h-BN.

To fully reveal the GB structures in CVD-grown h-BN, information on both grain scale and atomic scale is necessary. The former gives us the size, shape, and edge orientations of grains as well as GB morphology, while the latter provides information on the atomic structures. Herein, we use dark-field TEM (DF-TEM) and a scanning electron microscope (SEM) to obtain the general picture of GBs, combined with

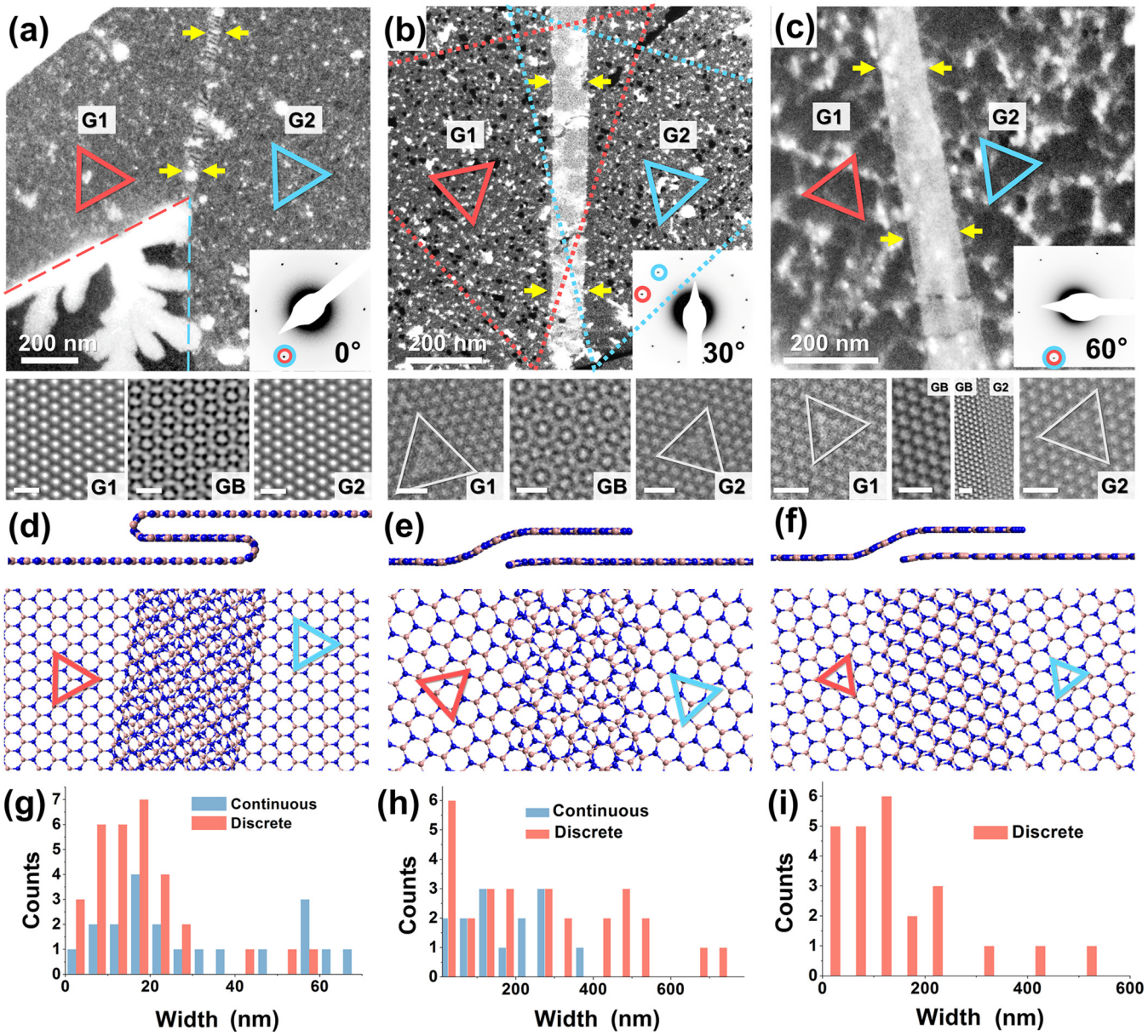

FIG. 2. (a)–(c) Dark-field TEM images of GBs with three typical misorientation angles: 0°, 30° (overlay of two DF images), and 60°, with their SAED inserted. The triangles represent their orientations, and colors indicate different grains, denoted $G1$ (grain 1) and $G2$ (grain 2). The yellow arrows indicate the positions of GBs. Their corresponding HRTEM images are shown below. Note that the atomic images in (a) are the inverse fast Fourier transform images. It should be noted that the diffraction spots of the interlayer in 0°-GB [inset in (a)] are invisible in SAED due to the rather weak small scattering intensity from the interlayer in the GB region. Scale bars for HRTEM images: 0.5 nm. (d)–(f) Cross-sectional (top) and planar (bottom) view of the corresponding structure model for GBs in (a)–(c). (g)–(i) Width distributions of three typical GBs. Due to the limited number of 60°-GBs observed in continuous films, the data of 60°-GBs in continuous films are not displayed here.

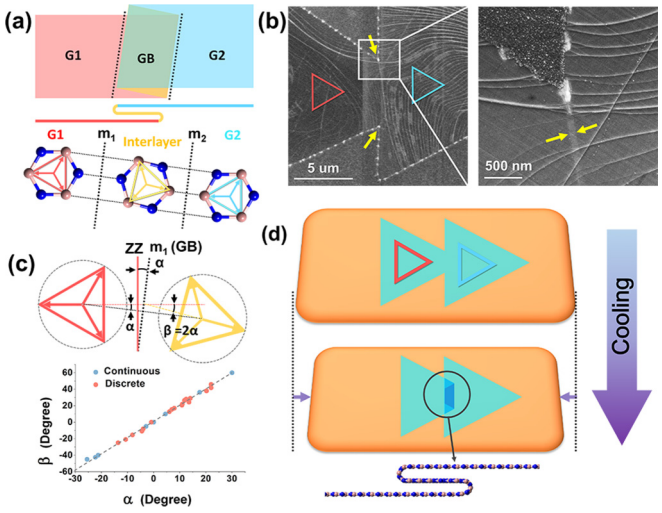

FIG. 3. (a) Schematic diagram of folded GBs in 0° and their structures of each layer with corresponding colors are shown at the bottom. The orange domain (the interlayer) is the reflection of the red (blue) domain with respect to the folded line m1 (m2), which is the GB direction. (b) Secondary-electron SEM images of the 0° GBs. (c) Geometrical relationships of folded GBs with a statistical plot of α and β values in GBs of two samples shown below. The formula of the dashed line is $\beta = 2\alpha$. (d) The folding process of the 0° GBs.

an atomically resolved HRTEM operating at 80 kV to get the detailed structures. The dark-field images and corresponding atomic resolution images of three representative GBs are displayed in Figs. 2(a)–2(c), with their atomic models shown in Figs. 2(d)–2(f), respectively. The orientations of grains are determined by analyzing the selected area electron diffraction (SAED) patterns, combined with the triangular silhouette as illustrated in Fig. 2(a), and together with the triangular holes with nitrogen-terminated zigzag edges caused by an electron beam with selected sputtering of boron atoms [40], as shown in the atomic images of Figs. 2(b) and 2(c). Two independent sets of diffraction spots with a 30° rotation angle are observed in Fig. 2(b). In contrast, there is only one set of diffraction spots in 0° and 60° GBs in Figs. 2(a) and 2(c), which indicates that two grains have the same or opposite orientations. Because the triangular silhouettes in Fig. 2(a) show the same orientation, the corresponding GB would have a 0° misorientation angle. In contrast, the two inverted triangular holes shown Fig. 2(c) indicate the inversion nature of two grains on two sides of the GB.

It is natural to propose that grains with the same orientation could coalesce and form a large single crystal with no line defects formed in between, if we ignore the relative sliding of the two grains [41]. Here, we demonstrate that even for grains without any relative rotation, there still exist imperfections with a width of tens of nanometers between two grains, and the corresponding atomic structure model is proposed as displayed in Fig. 2(d). The imperfections show a folded feature, which results in a relative rotation between the interlayer and two other layers. Furthermore, to verify the structure model in Fig. 2(d), we carry out a geometric analysis of the 0° GB. If the structure of the 0° GB is the same as sketched in Figs. 2(d) and 3(a), then the grains on two sides are the reflections of the interlayer with respect to the GB direction, as indicated at the bottom of Fig. 3(a). It is not difficult to resolve the geometrical relationship from Fig. 3(c) that $\beta = 2\alpha$, where α is the angle between the GB (marked by a black dotted line) and the zigzag boron direction (marked by a red line) of the left grain, and β is the angle between the interlayer in the folded area and the left grain. Please refer to Appendix B for a detailed angle definition. By statistically analyzing the angle relationships of the data shown in Fig. 3(c), where β is nearly twice as large as α, we confirm the folded nature of 0° GBs.

As for the case of neighboring grains with misorientation angles of 30° and 60°, OLGB with a finite width is observed, as indicated by atomic-scale images in Figs. 2(b) and 2(c). Moiré patterns along the GB are clearly seen in Fig. 2(b) due to the misorientation between two grains. The edges of the 30° GB are relatively straight and nearly parallel with each other, as revealed by the DF-TEM. However, they deviate from the direction of zigzag nitrogen-terminated edges marked as triangles with dashed lines in Fig. 2(b), which should be the growth front during CVD growth. As for neighboring grains with a misorientation angle of 60°, two edges with nitrogen termination should serve as the growth front of two grains, which are nearly atomically sharp and straight as seen in atomic scale HRTEM images in Fig. 2(c). The stacking order in the overlapping regions is assigned to be AA' (B is sitting right above N), which is reported to be the most energetically favorable configuration [42].

To have a comprehensive understanding of the formation process of these different GBs, we counted the width of three types of GBs in both discrete and continuous h-BN films, as summarized in Figs. 2(g)–2(i). Most of the 0° GBs have a width of 20 nm, and the maximum width is less than 70 nm, while the width of the 30° and 60° GBs mostly ranges from 100 to 500 nm. The distinctions in structure and width distributions between 0° GBs and 30° and 60° GBs indicate that 0° GBs have a different formation mechanism. It is inferred that the 0° GB structure should be caused by the compressive stress concentration around the connecting region of two h-BN grains during the cooling process after the high-temperature growth stage of h-BN, as illustrated in Fig. 3(d). This is due to the mismatch of the thermal expansion coefficient between h-BN (-3.5×10^{-6}/K at 800 K) [43] and the substrate (20×10^{-6}/K for Cu at 800 K) [44], resulting in a strain in h-BN as large as ~2% after cooling, supposing a growth temperature of 1000 °C. Thus, the 0° GBs are actually not GBs, and they are formed after the CVD growth. Such 0° GBs in h-BN are very similar to the wrinkles in graphene [45,46]. Nevertheless, other than the wrinkles inside the domains, which are distributed randomly in the films, the folding structures concentrate on the connecting regions, and they are much more likely to occur.

B. Formation mechanism of overlapping grain boundaries

There are no conventional CBGBs found in our data, in contrast to the cases of CVD-grown graphene and TMDs, where CBGBs account for a certain proportion [15,18]. For the consideration of generality, we also checked the h-BN samples grown on different substrates, such as polycrystalline Cu and liquid Cu substrate, which are also widely used in

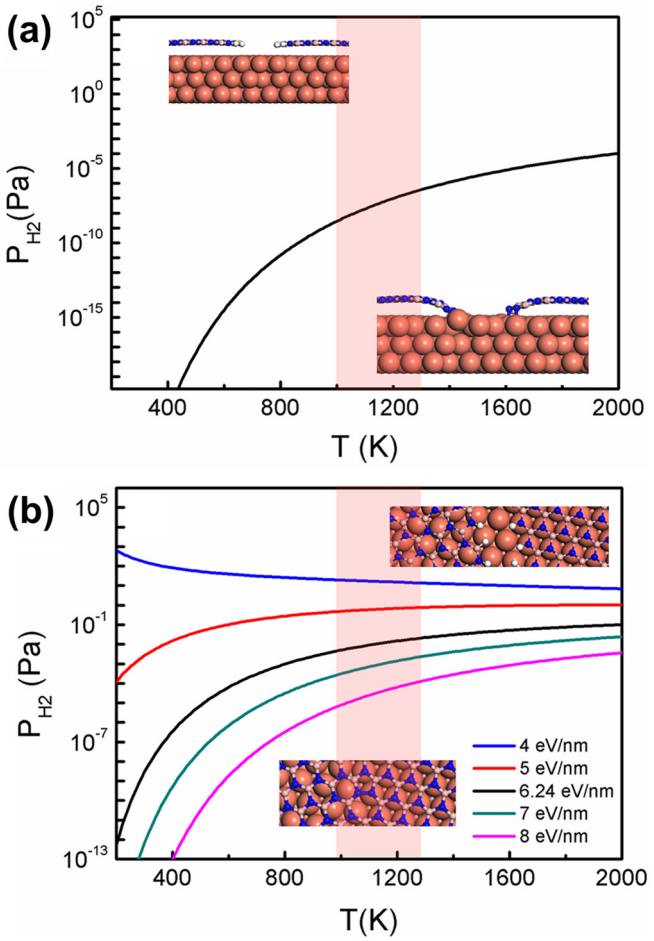

FIG. 4. (a) Thermodynamic diagrams between H-passivated h-BN edges and Cu substrate passivated h-BN edges. (b) Thermodynamic diagrams between H passivated h-BN edges and several covalently bonded GBs with different misorientation angles.

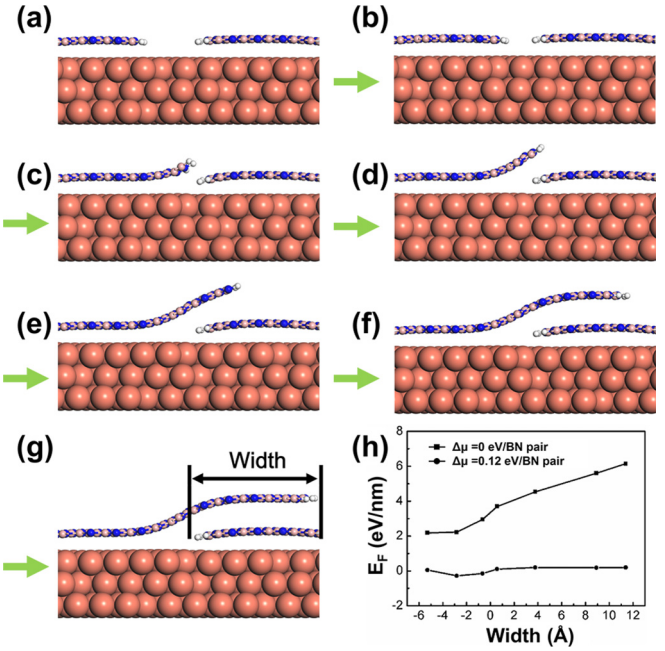

FIG. 5. (a)–(g) Formation process of overlapping GBs between two neighboring h-BN domains. (h) The formation energy evolution profile of (a)–(g).

CVD synthesis. As shown by Fig. 13 in Appendix C for the h-BN grown on polycrystalline Cu substrate, the GB structures exhibit the same feature as that found in h-BN on a Cu/Ni alloy (shown in Fig. 2): a folded interface for 0° GBs, and overlapping GBs for 30° GBs. This again proves the generality of our findings, irrespective of the choice of growth substrates, and other variant growth parameters.

To understand the formation mechanism of OLGBs, we further conduct DFT calculations. During the CVD growth process of h-BN, the growing edges should be passivated either by the metal atoms or by hydrogen atoms [47–50]. From our first-principles DFT calculations [Fig. 4(a)], it is found that the required H_2 partial pressure for passivating the h-BN edge on the Cu substrate in the typical growth temperature range (1000–1300 K) is quite low (10^{-8}–10^{-6} Pa). Due to the low content of Ni in the employed Cu-Ni alloy substrate, the edges of h-BN on Cu-Ni alloy substrates during its CVD growth process would be mostly passivated by H atoms, as in the case of a Cu substrate, which is the prerequisite for forming overlapping GBs. Furthermore, during the coalescence of neighboring h-BN grains, their edges would form either covalently bonded GBs by detaching H atoms or overlapping GBs through the climbing of one edge onto the other one, depending on their relative stabilities. Figure 4(b) shows the thermodynamic diagram between several covalently bonded h-BN GBs with different formation energies and H-passivated h-BN edges. Here, H-passivated h-BN edges were used to represent overlapping h-BN GBs. With the increase of the formation energy of h-BN covalently bonded GB from 4 to 8 eV/nm, the equilibrium H_2 partial pressure between overlapping h-BN GB and covalently bonded GB decreases sharply from 10 to 10^{-4} Pa. Since both previous reports [51] and our calculations demonstrate that most of the calculated covalently bonded GBs exhibits a higher formation energy at (and/or near to) 4 eV/nm (the formation energies of GBs are discussed in Appendix D), we can conclude that, under a H_2 partial pressure of $\geqslant$10 Pa, the majority of GBs in CVD h-BN would be overlapping GBs, consistent with our experimental findings. The absence of CBGBs in CVD-grown h-BN may be the reason why there are so few experimental studies on CBGBs in CVD-grown monolayer h-BN at an atomic scale [10,12]. However, it should be noted that covalently bonded GBs can also be formed if their formation energies are small enough (small-angle GBs) and the H_2 partial pressure is very low during the growth process.

Moreover, we studied the evolution of the formation energy during the process of an overlapping GB in h-BN. As shown in Fig. 5, the formation process can be divided into three stages: (i) the approaching of edges from neighboring domains [Figs. 5(a) and 5(b)] leads to little change of the formation energies, (ii) the climbing of one domain on another to form an overlapping structure [Figs. 5(c) and 5(d)] causes an increase of formation energy of about 2 eV/nm, and (iii) the elongation of the overlapping region [Figs. 5(e)–5(g)] results in a linear increase of the formation energy with a slope of about 2.3 eV/nm^2, due to the van der Waals interaction

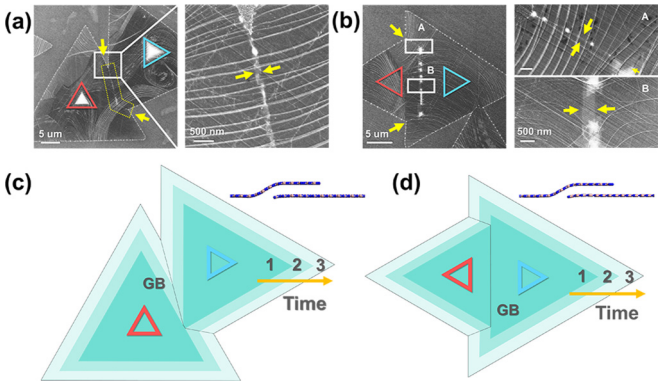

FIG. 6. (a), (b) Secondary-electron SEM images of 30° and 60° GBs. (c), (d) Schematic diagram for h-BN growth mechanism. The graduated color grains indicate the grains at different grow time.

difference between h-BN layers and h-BN-Cu substrate. This increase of the formation energy can be easily compensated by a very small growth driving force (0.12 eV per B-N pair) of h-BN during the CVD process, suggesting that overlapping GBs in h-BN are easily formed.

In short, the dominating H-passivated rather than metal-passivated edges in the growth process fulfill the prerequisite for forming OLGBs. Furthermore, the OLGBs are more thermodynamically favorable than most CBGBs under routine CVD synthesis.

C. Grain boundary formation at grain scale

At grain scale (tens of micrometers), the GB formation is a kinetic process, similar to that of MoS_2 [52]. As sketched in Figs. 6(c) and 6(d), two neighboring triangular grains first merged and continue to grow (as indicated by the graduated color), resulting in the formation of a boundary along intersections between two joint edges. The inclination of the GB then depends on the relative growth rates of the two grains. After the encounter of two neighboring grains, the growth of the climbing grain will stop when the OLGB reaches a certain width, which eventually leads to the appearance of parallel edges in OLGBs and GB morphology as shown in the Secondary-electron SEM images [Figs. 6(a) and 6(b)]. The strain induced by the cooling process will increase the width of the OLGBs, but it will not be the cause of the formation of OLGBs, due to the different magnitude of GB width between the 0° GBs and 30° (60°) GBs as illustrated in Figs. 2(g)–2(i). The width of 30° GBs does not increase with growth time, as the average width in continuous films is not larger than that in discrete films [Fig. 2(h)]. We infer two possible mechanisms of such a width-limited process. The first mechanism is that the overlapping layer grows between the catalyst (substrate) and the growing h-BN grain, and the feeding of the precursor comes through the edges of the upper h-BN layer [53], where the width of the OLGBs corresponds to the diffusion length of the precursor. The second mechanism is that after the overlapping layer grows onto another layer, the growth stops due to the absence of catalysis by the substrate. Further experiments and theoretical analyses are necessary to really understand this phenomenon and its mechanism.

IV. DISCUSSION

Our results demonstrate that the dominant GB structure in CVD-grown h-BN is overlapping GBs, rather than covalently bonded GBs. Its generality was also verified, via statistics of numerous GBs with different misorientation angles and GBs in samples grown on different substrates, and it was further revealed by thermodynamic diagrams via DFT calculations. This gives an entirely different view of GBs in h-BN and the 2D material family, because OLGB was usually regarded as a specific structure in 2D materials. Furthermore, our study provides a model for researchers to further explore the effects of GBs on properties. Since CVD is one of the most suitable methods for massive production of h-BN, such OLGBs should be given more attention and be considered when 2D membranes are used in industrial applications.

Moreover, though the tilt GBs will be excluded in large-area single-crystalline h-BN films prepared by coalescence of numerous grains grown from aligned h-BN nuclei, the wrinkling should still be considered. We revealed the folded structures (wrinkles) between two aligned grains by our atomic imaging method and statistics of the angles, which is instructive for further improving the performance of such films. Wrinkle-free 2D materials are mainly obtained by employing a substrate with similar thermal expansion to the 2D film. Jang *et al.* demonstrated wafer-scale wrinkle-free multilayer h-BN growth on a sapphire substrate by LPCVD [54], due to the small difference in the thermal expansion coefficients between h-BN and sapphire. Deng *et al.* proved that graphene is wrinkle-free grown on single-crystal Cu(111) thin film, due to the fact that Cu(111) is the lowest energy surface with the smallest thermal expansion among other crystallographic orientations, and larger interaction of graphene with Cu(111) than that of Cu(100) and Cu(110) [55].

From previous discussions, we could propose that we can change the GB structure by tuning the H_2 pressure. Moreover, when h-BN forms in-plane heterostructures with other 2D materials such as graphene, if they nucleate independently from each other, the edges of h-BN/graphene will be passivated either by H or by metal substrates, and will thus result in different interfaces. This can explain the formation of overlapping heterostructures between h-BN and graphene as previously observed [56]. However, the actual role of H_2 in the CVD process could be more complex than we expected. For instance, H_2 has a great impact on the growth speed and morphology of h-BN domains, and even has an etching effect on h-BN edges [57–59]. Thus, tuning the GB structures by either tuning H_2 or other methods should be systematically studied further. In addition, the energetic competition between CBGBs and OLGBs should exist in all 2D materials, including transition-metal dichalcogenides (TMDs). Though there is no hydrogen during some synthesis of TMDs, OLGBs are likely to form when OLGBs are much more energy favorable compared with CBGBs.

V. CONCLUSIONS

In summary, we have shown that overlapping GBs are the primary structure in CVD-grown h-BN, and there is a folded structure in two rotationally aligned grains. The theoretical

study shows that the edges of h-BN on CVD growth are dominantly passivated by H atoms, which is a precondition of forming overlapping GBs. In addition, we performed a systematic and theoretical study of an energetic competition between covalently bonded GBs and overlapping GBs. This study reveals the GB nature in CVD-grown h-BN and gives the mechanism behind the phenomenon, which will allow us to precisely control the growth of desired h-BN and other 2D materials.

ACKNOWLEDGMENTS

The authors thank Bin Wu, Zhepeng Zhang, and Yanfeng Zhang for providing us high-quality h-BN samples grown on liquid Cu and polycrystal Cu substrates for cross-checking, and we thank Xiaowei Wang, Xujing Ji, and Fenfa Yao for editing the manuscript and providing critical comments. This work was financially supported by the National Science Foundation of China under Grants No. 51772265, No. 51761165024, and No. 61721005, the National Basic Research Program of China under Grant No. 2015CB921004, and the 111 project under Grant No. B16042. The work on electron microscopy was carried out at the Center of Electron Microscopy of Zhejiang University. The work done in Korea was supported by Institute for Basic Science (IBS-R019-D1). The work performed at the Shanghai Institute of Microsystem and Information Technology, Chinese Academy of Sciences, was partially supported by the National Key R&D program under Grant No. 2017YFF0206106, the National Science Foundation of China under Grants No. 51772317 and No. 11604356, the China Postdoctoral Science Foundation under Grants No. 2017M621563 and No. 2018T110415, the Science and Technology Commission of Shanghai Municipality Grants No. 16ZR1442700 and No. 18511110700, and Shanghai Rising-Star Program (A type) under Grant No. 18QA1404800. The work done in Nanjing was supported by National Natural Science Foundation of China under Grants No. 51535005, No. 51472117, the Research Fund of State Key Laboratory of Mechanics and Control of Mechanical Structures (MCMS-I-0418K01, MCMS-I-0418Y01, MCMS-0417G02, MCMS-0417G03), the Fundamental Research Funds for the Central Universities (NP2017101, NC2018001), and a Project Funded by the Priority Academic Program Development of Jiangsu Higher Education Institutions.

X.R. and J.D. contributed equally to this work.

APPENDIX A: THE DEFINITION OF THE MISORIENTATION ANGLE

The misorientation angle θ is defined as the angle between two zigzag boron directions of left (red dashed line) and right (blue dashed line) grains, ranging from -60° to 60°. θ is positive if the vector from the red line (left grain) to the blue line (right grain) shows a clockwise rotation, as is shown in Fig. 7. It should be noted that 30° GB in the main text refers to both -30° GB and $+30^\circ$ GB following the definition mentioned above, while 60° GB only refers to 60° as defined here (-60° GB is barely found in our experiments).

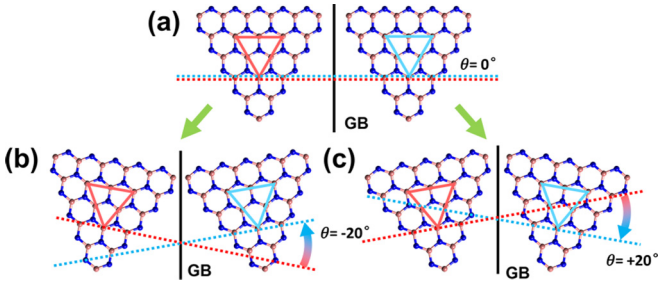

FIG. 7. The definition of misorientation angle θ.

APPENDIX B: DETAILED STRUCTURE DETERMINATION OF GRAIN BOUNDARIES

The data in Figs. 2(a) and 8 were acquired in a discrete sample on the ultrathin carbon film (to keep the triangle shape of h-BN grains). We cannot directly see the atomic structure from the images. However, there is a strong signal in FFT as seen in Fig. 8(d), which makes it easy to determine the orientations in the FFT and the layer number in inverse FFT images. Note that in inverse FFT images, it is improper to explore the detailed structures such as defect structures due to the artifacts resulting from the filtering process. The moiré patterns in Figs. 8(b), 8(c), and 8(e) are due to a small

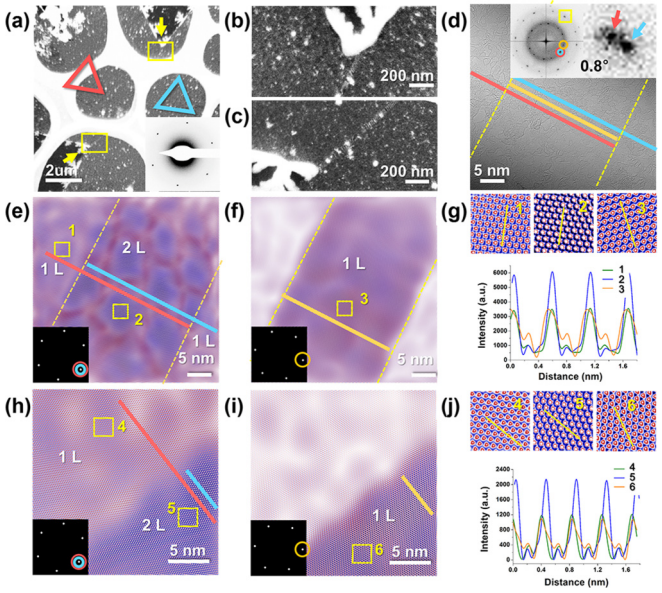

FIG. 8. (a) Dark-field image of 0° GBs, which is the same as Fig. 2(a) in main test (the image in the main text is rotated 40° anticlockwise for better display). (b), (c) Enlarged images, which are marked by orange rectangles. (d) HRTEM image of (b) and its corresponding FFT. The spot in red and blue circles is from the left and right domains, while the spot marked by the orange circle is from the interlayer. There is a small misorientation angle (0.8°) between the left and right domains as shown in the high-order FFT spots. (e), (f) Inverse FFT of the information of domains and the interlayer. Inserted: cut mask in FFT. (h), (i) Inverse FFT of HRTEM images in (c). Inserted: cut mask in FFT. (g), (j) The intensity profile of the corresponding region marked with numbers, which indicate the layer number of a certain region.

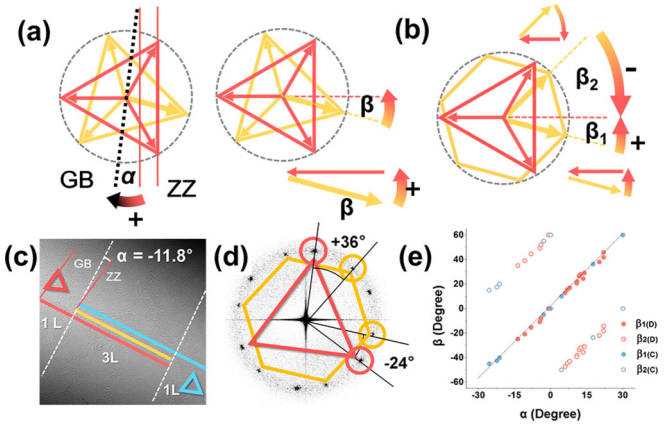

FIG. 9. (a) The definition of α and β. (b) Schematic diagram of the orientations of the interlayer (we can only get the orientation of a hexagonal lattice in the experiments) and the left grain, which shows two β values. (c) HRTEM image of 0° GB, which is the same as that in Fig. 8(d). Its corresponding FFT is displayed in (d). (e) The relationships between α and β (β_1 and β_2). D represents a discrete sample and C represents a continuous sample.

misorientation angle between the left and right grains in local area.

The 0° GBs are formed due to the folding process during the cooling, and they are actually not GBs but wrinkles. Such a folding process could also occur inside the grain. Thus we cannot determine whether the line defects in continuous film (which lost the triangular shape during grain coalescence) are the GBs between two grains or the wrinkles inside the grains. Nevertheless, the structures in continuous film also follow the same geometrical relationships as shown in Fig. 3(b), which indicates that they should be the same as the structure of 0° GBs in discrete samples.

A detailed angle definition in geometric analysis is displayed in Fig. 9. α is the angle between the GB line (marked by the black dotted line) and the zigzag boron direction (marked by the red line) of the left grain, which range from $-30°$ to 30° due to the symmetry of h-BN, and α is positive if the black line (GB) is in the clockwise direction from the red line. β is an angle of the interlayer (yellow) with respect to the left grain and in agreement with the vector relation, ranging from $-60°$ to 60°. β is positive if the vector displays an anticlockwise rotation.

In the experiments, we can determine the orientation of the left and right grains, and the orientation of the hexagonal lattice of the interlayer based on the FFT. However, we cannot distinguish the boron or nitride atoms in the hexagonal lattice of the interlayer. Therefore, the orientation of the interlayer is represented as a hexagon, which results in two β values, β_1 and β_2, as shown in Figs. 9(b) and 9(d) (+36° and $-24°$). The value of $-24°$ is around two times the angle of the GB with respect to the zigzag boron direction of the left grain ($-11.8°$), as shown in Fig. 9(c). The statistical analysis of α and two β values (β_1, β_2) is shown in Fig. 9(e), which indicates that only one β approximately satisfies the formula ($\beta = 2\alpha$). More details about 0° GBs are discussed in Figs. S3 and S4 in the Supplemental Material [37].

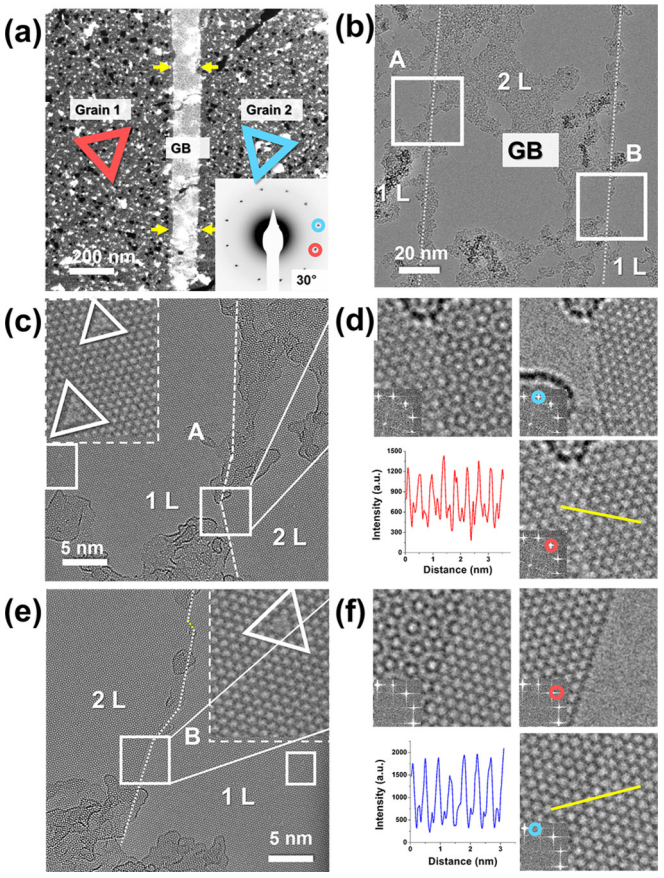

FIG. 10. Structure of 30° GB. (a) Dark-field image of 30° GB [the same as Fig. 2(b) in the main text]. (b) HRTEM image of low magnification, and detailed structures of local areas marked as A and B are displayed in (c) and (e). (d), (f) Inverse FFT of the local region in (c) and (e), with their masks inserted and an intensity profile in a certain region, which indicates the layer numbers. There are also some 30° GBs with ultranarrow width, as shown in Fig. S5 in the Supplemental Material [37].

The detailed structure of 30° GB is shown in Fig. 10. The edges of the 30° GB are relatively straight and nearly parallel with each other, as seen from the DF-TEM image [Fig. 2(b)] and the low-magnification TEM image [Fig. 11(a)], whose directions deviate from the direction of nitrogen-terminated zigzag edges marked by a blue line (growth front during CVD growth). However, when we look carefully at the edge, we find that the edges are formed by nitrogen-terminated steps,

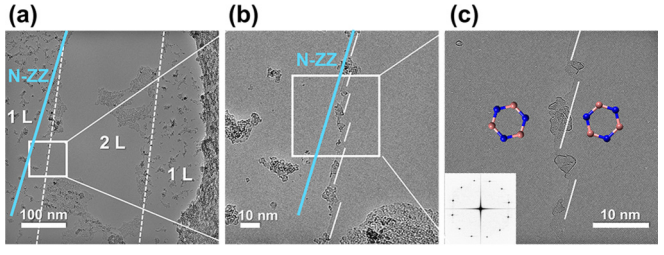

FIG. 11. (a) HRTEM image of 30° GBs. The blue line indicates the nitrogen-terminated zigzag edge. (b), (c) Local structures in (a), which show a steplike edge with straight edges terminated by nitrogen.

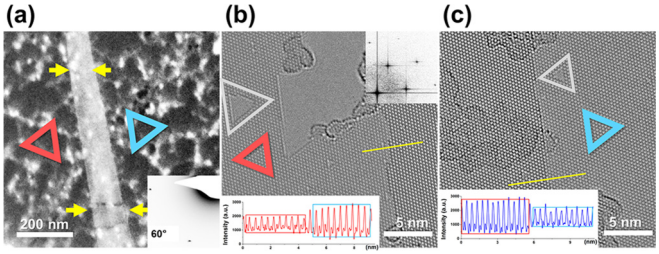

FIG. 12. (a) Dark field image of 60° GBs [the same as Fig. 2(c) in the main text]. (b), (c) The left and right regions of the grain boundary, and the intensity profile indicates the layer number of a certain region. 60° GB along other inclination is discussed in Fig. S6 in the Supplemental Material [37].

which further indicates the kinetic nature of GB formation. Moreover, the detailed structure of 60° GB is displayed in Fig. 12.

APPENDIX C: GRAIN BOUNDARIES IN H-BN ON POLYCRYSTALLINE COPPER

To overcome the variability of our findings, we also checked the h-BN samples grown on different substrates, such as polycrystalline Cu and liquid Cu substrate. The data of h-BN on polycrystalline Cu with two different growth times are shown in Fig. 13. Two h-BN samples were grown on a Cu substrate assisted with Cu vapor for different growth times [short-time and long-time growth as labeled in Figs. 13(e) and 13(f)], following a similar method to that in our previous work [60]. The results show no CBGBs found in our experiments.

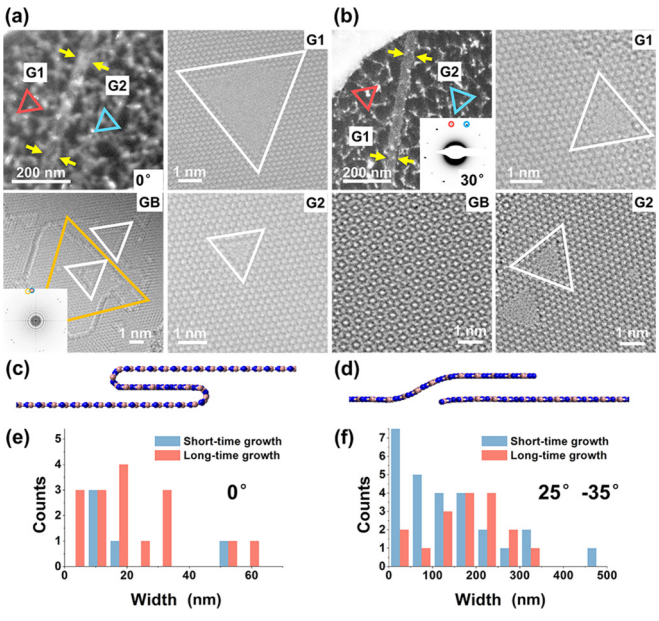

FIG. 13. Grain boundaries in h-BN on polycrystalline Cu. (a), (b) Dark-field TEM images of GBs with two typical misorientation angles: 0°, 30° (overlay of two DF images). The triangles represent their orientations, and colors indicate different grains denoted $G1$ (grain 1) and $G2$ (grain 2). Their corresponding HRTEM images are shown alongside. (c), (d) Cross-sectional view of the corresponding structure model for GBs in (a), (b). (e), (f) Width distributions of 0° and 25°–35° GBs.

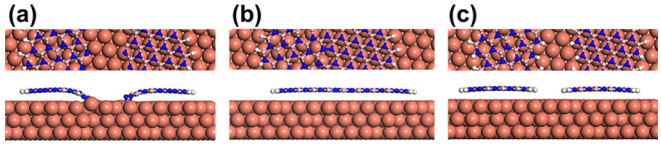

FIG. 14. (a) h-BN nanoribbons on a Cu substrate with both H-passivated edges and substrate-passivated edges, (b) h-BN nanoribbon on a Cu substrate with H-passivated edges and a twin GB, (c) h-BN nanoribbons on Cu substrates with only H-passivated edges.

APPENDIX D: COMPUTATIONAL DETAILS

1. Calculation of the formation energies of different types of h-BN edges on Cu substrate

The structures of different types of h-BN edges and covalently bonded GB are displayed in Fig. 14. The formation energy of the H-passivated h-BN edge is first calculated, which is defined by the following equation:

$$E_{F\text{-H}} = (E_T - E_S - N \times \varepsilon_{\text{BN}} - N_{\text{H}} \times \varepsilon_{\text{H2}}/2)/4l, \quad \text{(D1)}$$

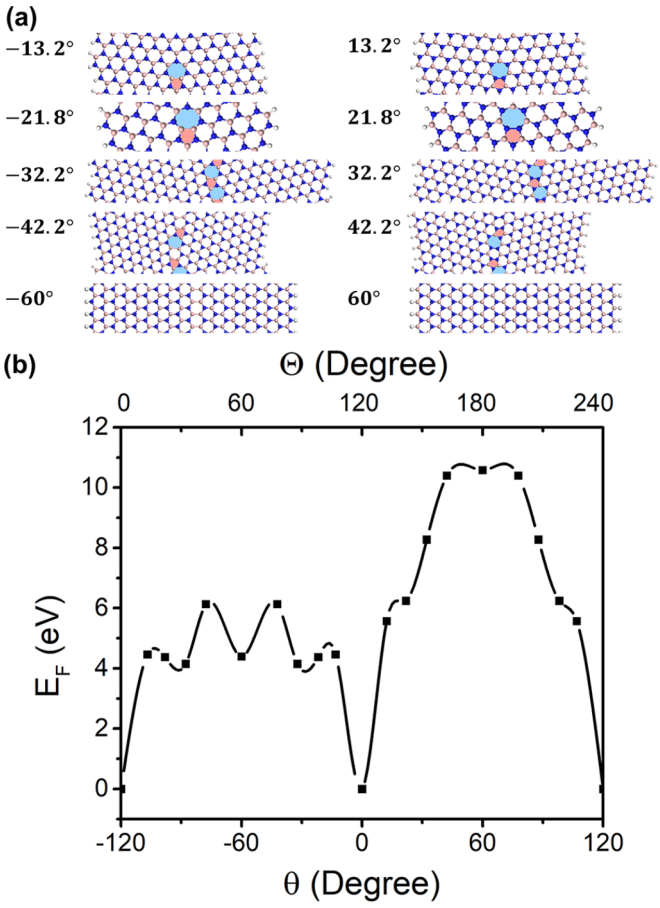

FIG. 15. Structures of covalently bonded GBs in h-BN with different misorientation angles θ and their corresponding formation energy. Θ in the top of (b) also represents the tilt angle between two grains, but is based on different reference line (Θ = 0 means two grains connected along armchair direction). Θ has the same definition as that in previous work [51].

where E_T and E_S are the energies of the total system and the substrate, respectively. N and N_{H} are the number of BN pairs and H atoms, respectively. $\varepsilon_{\mathrm{BN}}$ and $\varepsilon_{\mathrm{H2}}$ are the energies of a BN pair in h-BN on a Cu substrate and an H_2 molecule, respectively. L is the width of the unit cell.

The formation energy of a substrate-passivated h-BN edge is thus calculated by

$$E_{F\text{-}S} = [(E_T - E_S - N \times \varepsilon_{\mathrm{BN}} - N_{\mathrm{H}} \times \varepsilon_{\mathrm{H2}}/2)/l - 2 \times E_{F\text{-H}}]/2, \quad \text{(D2)}$$

and the formation energy of a covalently bonded GB in h-BN on a Cu substrate is

$$E_{F\text{-GB}} = (E_T - E_S - N \times \varepsilon_{\mathrm{BN}} - N_{\mathrm{H}} \times \varepsilon_{\mathrm{H2}}/2)/l - 2 \times E_{F\text{-H}}. \quad \text{(D3)}$$

2. Calculation of the formation energy evolution during the overlapping of two h-BN domains

The formation energy during the overlapping of two neighboring h-BN domains is calculated by

$$E_F = (E_T - E_S - N \times \varepsilon_{\mathrm{BN}} - N_{\mathrm{H}} \times \varepsilon_{\mathrm{H2}}/2)/l - 2E_{F\text{-H}} - N \times \Delta\mu_{\mathrm{BN}}, \quad \text{(D4)}$$

where $\Delta\mu_{\mathrm{BN}}$ is the chemical potential difference between a BN pair in h-BN on a Cu substrate and in a growth precursor.

3. Calculation of the chemical potential of H2 and thermodynamic diagrams

The hydrogen chemical potential μ_{H} in H_2 gas at a temperature T and a pressure P is calculated by [61]

$$\mu_{\mathrm{H}} = [E_{\mathrm{H2}} - k_B T \ln(g k_B T/P \times \xi_{\mathrm{trans}}\xi_{\mathrm{rot}}\xi_{\mathrm{vib}})]/2, \quad \text{(D5)}$$

where E_{H2} is the energy of a H_2 molecule; k_B is the Boltzmann constant; g equals 2 accounting for the degree of degeneracy of the electron energy level; and ξ_{trans}, ξ_{rot}, and ξ_{vib} are the partition functions of translation, rotation, and vibration motions. The thermodynamic diagrams between H-passivated h-BN edges and a covalently bonded grain boundary or Cu-passivated h-BN edges are obtained by calculating their Gibbs free-energy difference ΔG as

$$\Delta G = \Delta E_T + \Delta F_V - N_{\mathrm{H}} \times \mu_{\mathrm{H}}, \quad \text{(D6)}$$

where ΔE_T is the total energy difference between H-passivated h-BN edges and a covalently bonded grain boundary or Cu-passivated h-BN edges. ΔF_V is the vibration entropy difference between the H-passivated h-BN edges and a covalently bonded grain boundary or Cu-passivated h-BN edges.

4. Calculation of the formation energy of covalently bonded h-BN GBs as a function of its misorientation angle

To calculate the formation energy of covalently bonded GBs in h-BN as a function of its misorientation angle θ, twin GBs in h-BN are chosen. The GB formation energy is defined as

$$E_{F\text{-GB0}} = (E_T - N \times \varepsilon_{\mathrm{BN0}} - N_{\mathrm{H}} \times \varepsilon_{\mathrm{H2}}/2)/l - 2 \times E_{F\text{-H}}, \quad \text{(D7)}$$

where $\varepsilon_{\mathrm{BN0}}$ is the energy of a BN pair in suspended h-BN. The calculated GB formation energy profile is shown in Fig. 15.

[1] K. S. Novoselov, V. I. Fal'ko, L. Colombo, P. R. Gellert, M. G. Schwab, and K. Kim, Nature (London) **490**, 192 (2012).

[2] M. Xu, T. Liang, M. Shi, and H. Chen, Chem. Rev. **113**, 3766 (2013).

[3] G. R. Bhimanapati, Z. Lin, V. Meunier, Y. Jung, J. Cha, S. Das, D. Xiao, Y. Son, M. S. Strano, V. R. Cooper, L. Liang, S. G. Louie, E. Ringe, W. Zhou, S. S. Kim, R. R. Naik, B. G. Sumpter, H. Terrones, F. Xia, Y. Wang, J. Zhu, D. Akinwande, N. Alem, J. A. Schuller, R. E. Schaak, M. Terrones, and J. A. Robinson, ACS Nano **9**, 11509 (2015).

[4] A. K. Geim and I. V. Grigorieva, Nature (London) **499**, 419 (2013).

[5] K. S. Novoselov, A. Mishchenko, A. Carvalho, and A. H. Castro Neto, Science **353**, aac9439 (2016).

[6] X. Li, W. Cai, J. An, S. Kim, J. Nah, D. Yang, R. Piner, A. Velamakanni, I. Jung, E. Tutuc, S. K. Banerjee, L. Colombo, and R. S. Ruoff, Science **324**, 1312 (2009).

[7] Y. Shi, C. Hamsen, X. Jia, K. K. Kim, A. Reina, M. Hofmann, A. L. Hsu, K. Zhang, H. Li, Z.-Y. Juang, M. S. Dresselhaus, L.-J. Li, and J. Kong, Nano Lett. **10**, 4134 (2010).

[8] Y.-H. Lee, X.-Q. Zhang, W. Zhang, M.-T. Chang, C.-T. Lin, K.-D. Chang, Y.-C. Yu, J. T.-W. Wang, C.-S. Chang, L.-J. Li, and T.-W. Lin, Adv. Mater. **24**, 2320 (2012).

[9] P. Y. Huang, C. S. Ruiz-Vargas, A. M. van der Zande, W. S. Whitney, M. P. Levendorf, J. W. Kevek, S. Garg, J. S. Alden, C. J. Hustedt, Y. Zhu, J. Park, P. L. McEuen, and D. A. Muller, Nature (London) **469**, 389 (2011).

[10] A. L. Gibb, N. Alem, J.-H. Chen, K. J. Erickson, J. Ciston, A. Gautam, M. Linck, and A. Zettl, J. Am. Chem. Soc. **135**, 6758 (2013).

[11] O. Cretu, Y.-C. Lin, and K. Suenaga, Nano Lett. **14**, 1064 (2014).

[12] Q. Li, X. Zou, M. Liu, J. Sun, Y. Gao, Y. Qi, X. Zhou, B. I. Yakobson, Y. Zhang, and Z. Liu, Nano Lett. **15**, 5804 (2015).

[13] X. Zou, Y. Liu, and B. I. Yakobson, Nano Lett. **13**, 253 (2013).

[14] A. W. Tsen, L. Brown, M. P. Levendorf, F. Ghahari, P. Y. Huang, R. W. Havener, C. S. Ruiz-Vargas, D. A. Muller, P. Kim, and J. Park, Science **336**, 1143 (2012).

[15] J. Dong, H. Wang, H. Peng, Z. Liu, K. Zhang, and F. Ding, Chem. Sci. **8**, 2209 (2017).

[16] A. W. Robertson, A. Bachmatiuk, Y. A. Wu, F. Schäffel, B. Rellinghaus, B. Büchner, M. H. Rümmeli, and J. H. Warner, ACS Nano **5**, 6610 (2011).

[17] B. C. Bayer, S. Caneva, T. J. Pennycook, J. Kotakoski, C. Mangler, S. Hofmann, and J. C. Meyer, ACS Nano **11**, 4521 (2017).

[18] A. M. van der Zande, P. Y. Huang, D. A. Chenet, T. C. Berkelbach, Y. You, G.-H. Lee, T. F. Heinz, D. R. Reichman, D. A. Muller, and J. C. Hone, Nat. Mater. **12**, 554 (2013).

[19] S. Najmaei, Z. Liu, W. Zhou, X. Zou, G. Shi, S. Lei, B. I. Yakobson, J.-C. Idrobo, P. M. Ajayan, and J. Lou, Nat. Mater. **12**, 754 (2013).

[20] G.-H. Lee, R. C. Cooper, S. J. An, S. Lee, A. van der Zande, N. Petrone, A. G. Hammerberg, C. Lee, B. Crawford, and W. Oliver, Science **340**, 1073 (2013).

[21] M. Becton and X. Wang, Phys. Chem. Chem. Phys. **17**, 21894 (2015).

[22] N. Ding, C.-M. L. Wu, and H. Li, Phys. Chem. Chem. Phys. **16**, 23716 (2014).

[23] L. Song, L. Ci, H. Lu, P. B. Sorokin, C. Jin, J. Ni, A. G. Kvashnin, D. G. Kvashnin, J. Lou, B. I. Yakobson, and P. M. Ajayan, Nano Lett. **10**, 3209 (2010).

[24] T. Ouyang, Y. Chen, Y. Xie, K. Yang, Z. Bao, and J. Zhong, Nanotechnology **21**, 245701 (2010).

[25] D. Golberg, Y. Bando, Y. Huang, T. Terao, M. Mitome, C. Tang, and C. Zhi, ACS Nano **4**, 2979 (2010).

[26] Y. Chen, J. Zou, S. J. Campbell, and G. Le Caer, Appl. Phys. Lett. **84**, 2430 (2004).

[27] Y. Kubota, K. Watanabe, O. Tsuda, and T. Taniguchi, Science **317**, 932 (2007).

[28] C. R. Dean, A. F. Young, I. Meric, C. Lee, L. Wang, S. Sorgenfrei, K. Watanabe, T. Taniguchi, P. Kim, K. L. Shepard, and J. Hone, Nat. Nanotech. **5**, 722 (2010).

[29] J. Xue, J. Sanchez-Yamagishi, D. Bulmash, P. Jacquod, A. Deshpande, K. Watanabe, T. Taniguchi, P. Jarillo-Herrero, and B. J. LeRoy, Nat. Mater. **10**, 282 (2011).

[30] G. Lu, T. Wu, Q. Yuan, H. Wang, H. Wang, F. Ding, X. Xie, and M. Jiang, Nat. Commun. **6**, 6160 (2015).

[31] Y. Wang, Y. Zheng, X. Xu, E. Dubuisson, Q. Bao, J. Lu, and K. P. Loh, ACS Nano **5**, 9927 (2011).

[32] G. Kresse and J. Hafner, Phys. Rev. B **48**, 13115 (1993).

[33] G. Kresse and J. Furthmüller, Comput. Mater. Sci. **6**, 15 (1996).

[34] G. Kresse and D. Joubert, Phys. Rev. B **59**, 1758 (1999).

[35] J. P. Perdew, K. Burke, and M. Ernzerhof, Phys. Rev. Lett. **77**, 3865 (1996).

[36] S. Grimme, J. Comput. Chem. **27**, 1787 (2006).

[37] See Supplemental Material at http://link.aps.org/supplemental/10.1103/PhysRevMaterials.3.014004 for additional information about the experimental results.

[38] Y. Liu, S. Bhowmick, and B. I. Yakobson, Nano Lett. **11**, 3113 (2011).

[39] G. E. Wood, A. J. Marsden, J. J. Mudd, M. Walker, M. Asensio, J. Avila, K. Chen, G. R. Bell, and N. R. Wilson, 2D Mater. **2**, 025003 (2015).

[40] J. C. Meyer, A. Chuvilin, G. Algara-Siller, J. Biskupek, and U. Kaiser, Nano Lett. **9**, 2683 (2009).

[41] J. Li, Y. Li, J. Yin, X. Ren, X. Liu, C. Jin, and W. Guo, Small **12**, 3645 (2016).

[42] O. Hod, J. Chem. Theor. Comput. **8**, 1360 (2012).

[43] Y. Mishin, M. J. Mehl, D. A. Papaconstantopoulos, A. F. Voter, and J. D. Kress, Phys. Rev. B **63**, 224106 (2001).

[44] S. Thomas, K. M. Ajith, S. Chandra, and M. C. Valsakumar, J. Phys.: Condens. Matter **27**, 315302 (2015).

[45] K. Kim, Z. Lee, B. D. Malone, K. T. Chan, B. Alemán, W. Regan, W. Gannett, M. F. Crommie, M. L. Cohen, and A. Zettl, Phys. Rev. B **83**, 245433 (2011).

[46] W. Zhu, T. Low, V. Perebeinos, A. A. Bol, Y. Zhu, H. Yan, J. Tersoff, and P. Avouris, Nano Lett. **12**, 3431 (2012).

[47] R. Zhao, F. Li, Z. Liu, Z. Liu, and F. Ding, Phys. Chem. Chem. Phys. **17**, 29327 (2015).

[48] X. Zhang, L. Wang, J. Xin, B. I. Yakobson, and F. Ding, J. Am. Chem. Soc. **136**, 3040 (2014).

[49] H. Wang, X. Xu, J. Li, L. Lin, L. Sun, X. Sun, S. Zhao, C. Tan, C. Chen, W. Dang, H. Ren, J. Zhang, B. Deng, A. L. Koh, L. Liao, N. Kang, Y. Chen, H. Xu, F. Ding, K. Liu, H. Peng, and Z. Liu, Adv. Mater. **28**, 8968 (2016).

[50] H. Shu, X. Chen, and F. Ding, Chem. Sci. **5**, 4639 (2014).

[51] Y. Liu, X. Zou, and B. I. Yakobson, ACS Nano **6**, 7053 (2012).

[52] J. Cheng, T. Jiang, Q. Ji, Y. Zhang, Z. Li, Y. Shan, Y. Zhang, X. Gong, W. Liu, and S. Wu, Adv. Mater. **27**, 4069 (2015).

[53] P. R. Kidambi, R. Blume, J. Kling, J. B. Wagner, C. Baehtz, R. S. Weatherup, R. Schloegl, B. C. Bayer, and S. Hofmann, Chem. Mater. **26**, 6380 (2014).

[54] A.-R. Jang, S. Hong, C. Hyun, S. I. Yoon, G. Kim, H. Y. Jeong, T. J. Shin, S. O. Park, K. Wong, S. K. Kwak, N. Park, K. Yu, E. Choi, A. Mishchenko, F. Withers, K. S. Novoselov, H. Lim, and H. S. Shin, Nano Lett. **16**, 3360 (2016).

[55] B. Deng, Z. Pang, S. Chen, X. Li, C. Meng, J. Li, M. Liu, J. Wu, Y. Qi, W. Dang, H. Yang, Y. Zhang, J. Zhang, N. Kang, H. Xu, Q. Fu, X. Qiu, P. Gao, Y. Wei, Z. Liu, and H. Peng, ACS Nano **11**, 12337 (2017).

[56] S. M. Kim, A. Hsu, P. T. Araujo, Y.-H. Lee, T. Palacios, M. Dresselhaus, J.-C. Idrobo, K. K. Kim, and J. Kong, Nano Lett. **13**, 933 (2013).

[57] P. Sutter, J. Lahiri, P. Albrecht, and E. Sutter, ACS Nano **5**, 7303 (2011).

[58] L. Wang, B. Wu, L. Jiang, J. Chen, Y. Li, W. Guo, P. Hu, and Y. Liu, Adv. Mater. **27**, 4858 (2015).

[59] Y. Y. Stehle, X. Sang, R. R. Unocic, D. Voylov, R. K. Jackson, S. Smirnov, and I. Vlassiouk, Nano Lett. **17**, 7306 (2017).

[60] J. Yin, J. Yu, X. Li, J. Li, J. Zhou, Z. Zhang, and W. Guo, Small **11**, 4497 (2015).

[61] L. D. Landau and E. M. Lifshitz, *Statistical Physics* (Butterworth-Heinemann, Oxford, 1980).